Measurement and verification of a 6G terahertz multi-mode tunable metasurface based on multiferroic materials and optimize its sensing performance

JIANFANG DENG[1,*], HONGLIANG ZHANG[2], RUI TIAN[3]
[1]*Nanjing Vocational Institute of Railway Technology, School of Communication and Signal, Jiangsu, Nanjing, 210031, China*
[2]*Nanjing Metro Group Co., Ltd., Signal and Communication Branch, Jiangsu, Nanjing, 211135, China*
[3]*Lanzhou Jiaotong University, Key Lab of Opt-Electronic Technology and Intelligent Control of Ministry of Education, Gansu, Lanzhou, 730070, China*

Here, a 6G terahertz multimodal tunable metasurface based on multiferroic materials is proposed and verified. In the range of 0.3-4.5THz, four absorption peaks based on the bright-dark mode coupling effect between the disc metal arrays were obtained. The absorption performance of this metasurface sample shows geometric parameter selectivity (disc diameter and dielectric layer thickness). In detailed measurements of sensing performance and tunable performance, the metasurface sample demonstrated significant temperature sensitivity. These measurement results provide a foundation for the development of 6G optoelectronic devices based on metasurfaces.

(Received December 23, 2024; accepted August 5, 2025)

Keywords: Metasurface, Multiferroic materials, 6G, Terahertz, Sensing, Metamaterials

1. Introduction

In the past two decades, electromagnetic metasurfaces/metamaterials based on periodic micro-nano structures at sub-wavelength sizes have been widely reported and verified [1-6]. These electromagnetic metasurfaces/metamaterials reveal many interesting resonant behaviors and are applied in numerous fields, such as sensing, control, transformation, field enhancement, etc [7-11]. Among them, the electromagnetic metasurface/metamaterial filter is an anticipated photoelectric device [12-14]. On the one hand, with the development of preparation techniques and theories, the functions of electromagnetic metasurface/metamaterial filters have been rapidly expanded. On the other hand, numerous theories have been proposed and applied by researchers to explain the resonance behavior of electromagnetic metasurface/metamaterial filters, such as transmission line theory, interference theory, etc [12-14]. However, with the expansion of application scope, the development of metasurfaces faces challenges. Traditional metasurface filters are difficult to achieve multi-mode modulation of working frequencies and cannot meet the requirements in the fields of 5G and 6G wireless communication. In the field of 6G wireless communication, electromagnetic metasurface/metamaterial filters need to have characteristics such as multi-mode resonance, wide frequency range modulation, miniaturization, low power consumption, and high Q value, so as to meet diverse filtering requirements [15-16]. In recent years, numerous metasurface/metamaterial filters have achieved multi-mode resonance, tunability and other performances [17-18]. Two strategies were proposed by researchers and used to expand the resonance performance of electromagnetic metasurface/metamaterial filters: On the one hand, tunable dielectric layers are increasingly being applied by researchers to the structural strategies of electromagnetic metasurface/metamaterial filters. For example, vanadium dioxide, graphene, multiferroic materials (BiFeO3, BFO), etc [19-21]. The characteristic of these medium layers is that the resonant state depends on the external control conditions. On the other hand, phase change materials like Ge2Sb2Te5 (GST) have also been applied in structural strategies. The phase transition state of the GST layer does not depend on external temperature conditions.

Here, a 6G terahertz metasurface based on multiferroic materials and GST materials was proposed and its sensing performance was measured. This metasurface is capable of obtaining four distinct resonance modes within the range of 0.3-4.5THz, thereby achieving

four filtering Windows. These filter bands are based on the coupling effect of multiple resonant modes. In addition, the resonant properties (frequency, amplitude) of these filter bands can be modulated by changing the temperature conditions. These measurement results verify the tunability and multi-resonance mode performance of the 6G terahertz metasurface.

2. Structure and experiments

This 6G terahertz metasurface consists of four layers of materials: the top and bottom layers are the same array of metal discs, and the middle layers are the GST layer and the multiferroic material BFO layer, as shown in Fig. 1 (a). The geometric parameters of this structure are as follows: the lattice constant P=10 microns, the diameter of the disk array d=8 microns, and the thickness of the material is: t1=2 microns, t2=5 microns, t3=7 microns. The simulation results of this metasurface were obtained by using the software HFSS. The simulation process adopts an ideal electromagnetic boundary, with the distances from the excitation port and the receiving port to the unit being 10 microns and 6 microns respectively. The step size of the scanning frequency was set to 0.001THz. All the samples were prepared and measured by the following steps: (a) A vacuum coating device (ZZL-U400C) covered a layer of metal on the surface of a temporary substrate; (b) After the first layer of metal is cooled, the vacuum coating equipment (ZZL-U400C) covers a layer of multiferroic material BFO on the surface of a layer of metal; (c) After the BFO layer is cooled, the vacuum coating equipment (ZZL-U400C) covers a layer of GST on the surface of the BFO layer; (d) After the GST layer is cooled, the vacuum coating equipment (ZZL-U400C) covers the surface of the GST layer with the second layer of metal; (e) The Etching device CABL-9000C is used to prepare the top and bottom metal disc arrays, as shown in Fig. 1 (b). Bruker Optics Equinox obtained the absorption spectra of the samples, as shown in Fig. 2.

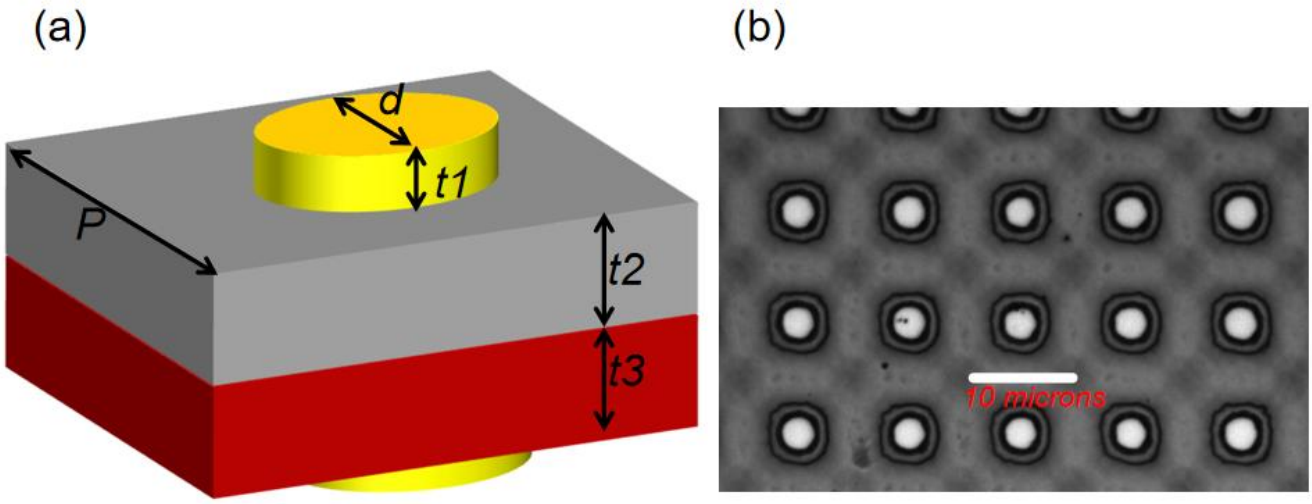

Fig. 1. (a) The structural strategy of this metasurface. (b)A photo of the metasurface sample (colour online)

3. Results

The measurement results and simulation results of the absorption rate of this metasurface are presented in Fig. 2. Four resonant absorption peaks were excited and marked as: P1, P2, P3, P4. The measured amplitudes are: 0.811, 0.722, 0.663, 0.764, and the resonance positions are: 1.07THz, 1.756THz, 2.708THz, 3.416THz, as shown in Fig. 2 (a). The simulated amplitudes are: 0.821, 0.728, 0.683, 0.781, and the resonance positions are: 1.12THz, 1.766THz, 2.713THz, 3.456THz, as shown in Fig. 2 (b). The amplitude errors are: 0.02, 0.006, 0.02, 0.017, and the resonance position errors are: 0.05THz, 0.01THz, 0.005THz, 0.04THz, as shown in Fig. 2. By comparing these results, it can be known that the calculation conditions adopted in the simulation process are close to the resonant properties of the actual samples. Outside these absorption bands, the average absorption rate of the sample is approximately 0.056.

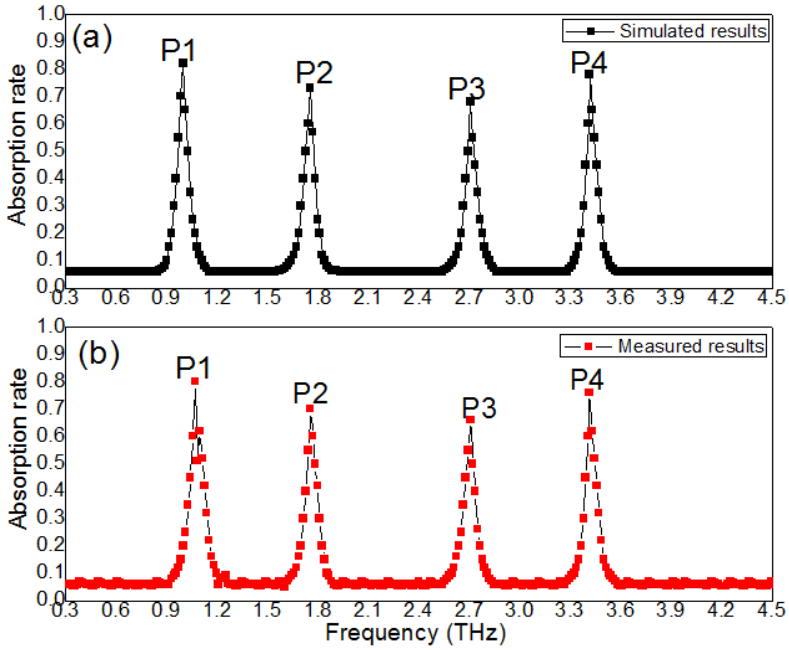

Fig. 2. (a) The measured absorption spectrum. (b)The absorption spectrum obtained through simulation (colour online)

To intuitively understand the resonance characteristics of this metasurface, the distribution of electric field intensity at four resonance positions was simulated and presented in Figs. 3 and 4. At the resonant position 1.07THz (P1), the bright mode resonates are excited at the edges of the disc arrays A and C. Meanwhile, dark modes were found at the edges of the disc arrays B and D, as shown in Fig. 3 (a). Within the same Unit (Unit 1 or Unit 2), a significant bright-dark coupling resonance behavior is formed between the bright mode above and the dark mode below, thereby obtaining the PIT effect, as shown in Fig. 3 (a). These bright-dark coupling resonance behaviors improve the electromagnetic wave impedance matching conditions of the sample near the resonance position 1.07THz, thereby enhancing the absorption performance of the sample and exciting the absorption peak P1, as shown in Fig. 3 (a). At the resonance position 1.756THz (P2), the bright mode resonates at the edges of disk arrays B and D, and the dark mode is found at the edges of disk arrays A and C, as shown in Fig. 3 (b), which is not consistent with the resonance position of P1.

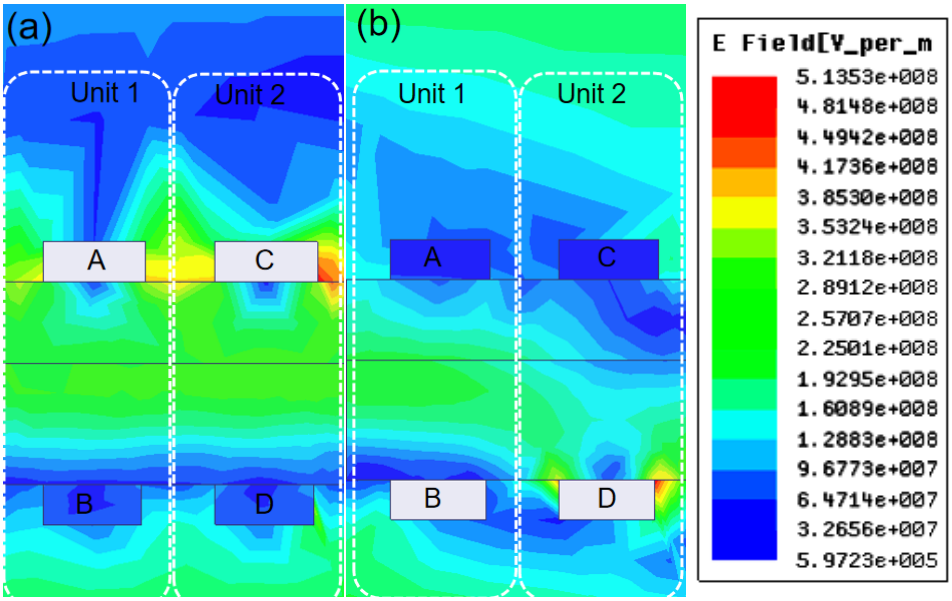

Fig. 3. Simulated electric fields: (a) 1.07THz, (b) 1.756THz (colour online)

A strong bright-dark coupling resonance is obtained within the same Unit (Unit 1 or Unit 2), and thereby excites the absorption peak P2. It should be pointed out that the coupling directions of absorption peaks P1 and P2 are opposite, as shown in Fig. 3 (a-b). The simulation results in Fig. 3 verify the significant role of the bright-dark coupling resonance behavior based on the PIT effect in enhancing the absorption performance.

The electric field intensities of the absorption peaks P3 and P4 are shown in Fig. 4. At the resonant position 2.708THz (P3), the bright mode resonates at the edges of the disk arrays A and D. Meanwhile, dark modes were found at the edges of the disc arrays B and C, as shown in Fig. 4 (a). Between the adjacent units (Unit 1 and Unit 2), a horizontal bright-dark coupling resonance behavior is formed between the bright mode and the dark mode, thereby obtaining the PIT effect, as shown in Fig. 4 (a). These bright-dark coupling resonance behaviors improve the electromagnetic wave impedance matching conditions of the sample near the resonance position of 2.708THz. The absorption performance of the sample was synchronously enhanced, thereby exciting the absorption peak P3, as shown in Fig. 4 (a). At the resonance position 3.416THz (P4), the bright mode resonates at the edges of disc arrays A and B, and the dark mode is found at the edges of disc arrays C and D, as shown in Fig. 4 (b). Strong bright-dark coupling resonances are acquired within adjacent units (Unit 1 and Unit 2), and thereby the absorption peak P4 is excited.

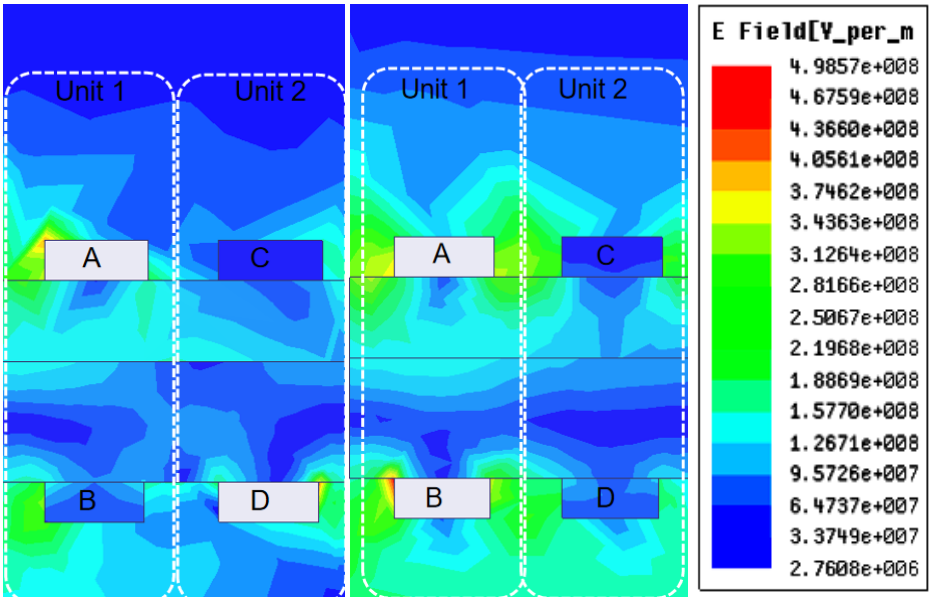

Fig. 4. Simulated electric fields: (a) 2.708THz, (b)3.416THz (colour online)

To understand the electromagnetic resonance performance of this metasurface, the equivalent medium theory was used to calculate the equivalent parameters and resonance frequencies of the metasurface structure. During the calculation process, the metal disc array is described using the Drude pattern [22]:

$$\varepsilon(\omega)=1-\frac{\omega_p^2}{\omega^2-i\omega\gamma_D} \tag{1}$$

In the above formula, the parameters of the metal layer are: $\gamma_D=9\times10^{13}s^{-1}$ and $\omega_P=1.37\times10^{16}s^{-1}$. The medium layer GST can be described by the following equations [23]:

$$a_m=\frac{[D_m(nKR)/n+m/kR]\psi_m(kR)-\psi_{m-1}(kR)}{[D_m(nKR)/n+m/kR]\xi_m(kR)-\xi_{m-1}(kR)} \tag{2}$$

$$b_m=\frac{[nD_m(nKR)/n+m/kR]\psi_m(kR)-\psi_{m-1}(kR)}{[nD_m(nKR)/n+m/kR]\xi_m(kR)-\xi_{m-1}(kR)} \tag{3}$$

$$Q_{scat}=\frac{2}{k^2R^2}\sum_{m=1}^{\infty}(2l+1)[|a_m|^2+|b_m|^2] \tag{4}$$

$$D_m(nKR)=\psi'(nkR)/\psi(nkR) \tag{5}$$

$$\frac{\varepsilon(\lambda,C)-1}{\varepsilon(\lambda,C)+2}=C\times\frac{\varepsilon_C(\lambda)-1}{\varepsilon_C(\lambda)+2}+(1-C)\times\frac{\varepsilon_a(\lambda)-1}{\varepsilon_a(\lambda)+2} \tag{6}$$

The equivalent dielectric constant, equivalent magnetic permeability and equivalent refractive index of this metasurface element are [24]:

$$\varepsilon_{eff}(f) = \varepsilon_0(\varepsilon_\infty - \frac{c_0^2 / f_e^2}{c_0^2 / f^2 - jc_0\gamma_e / f}) \tag{7}$$

$$\mu_{eff}(f) = \mu_0(1 - \sum_i^2 \frac{F_i f_e^2}{f^2 - f^2{}_{mi} - j\gamma_e f_{mi}}) \tag{8}$$

$$n_{eff}(f) = \sqrt{\mu_{eff}(f)}\sqrt{\varepsilon_{eff}(f)} \tag{9}$$

According to the equivalent refractive index of the metasurface unit cell, the resonant frequency can be expressed as [25]:

$$f = \frac{m - \Psi / \pi}{2\,\mathrm{Re}(n_{eff})d} \tag{10}$$

According to the equivalent medium theory, the resonant frequencies of this metasurface unit within the working frequency band are: 1.131THz, 1.739THz, 2.711THz, 3.412THz. The errors between these calculation results and measurement results are: 0.061THz, 0.017THz, 0.003THz, 0.004THz. These errors fall within a reasonable range, and the electromagnetic and electromagnetic resonance properties of the metasurface sample conform to the equivalent medium theory. The boundaries of the metasurface units are set according to the reported achievements [26].

The electric field intensity distribution of the metasurface sample near four resonant positions was obtained through the software HFSS, as shown in Figs. 3 and 4. These simulated electric fields visually reveal that the physical mechanisms of the four absorption peaks are all based on the bright-dark mode coupling effect between the disc metal arrays (including: coupling within the same element and coupling between adjacent elements). The bright-dark mode coupling effect among these disc metal arrays is directly related to the structural parameters of the metasurface. To optimize the performance of the metasurface, in the subsequent detailed measurements, the diameter d of the metal disc was gradually increased to obtain the detailed absorption performance of the metasurface, as shown in Fig. 5. The diameter d of the metal disc is gradually increased (the temperature during the measurement process is at room temperature). The four absorption peaks were gradually strengthened and moved to the low-frequency region, as shown in Fig. 5. Therefore, the performance of the metasurface can be modulated by changing the diameter d of the metal disc. This enhancement effect is related to the resonance mechanism of the absorption peak. For example, the absorption peak P1, at the resonant position 1.07THz, within the same unit, the bright-dark coupling effect is excited between the upper and lower metal disc arrays, as shown in Fig. 3 (a). With the increase of the diameter d of the metal disc, the effective coupling area between the upper and lower metal disc arrays is rapidly increased (the coupling distance between the bright mode and the dark mode is not changed), thereby resulting in the synchronous enhancement of the bright-dark coupling effect. Therefore, in Fig. 5, the amplitude of the absorption peak P1 increases rapidly with the increase of the diameter d of the metal disc. For example, the absorption peak P2, at the resonance position 1.756THz, within the same unit, the bright-dark coupling effect is excited between the upper and lower metal disc arrays (the coupling direction is from bottom to top, opposite to the coupling direction in Fig. 3 (a)), as shown in Fig. 3 (b). With the increase of the diameter d of the metal disc, the effective area of the bright-dark coupling effect between the upper and lower metal disc arrays is also increased. Therefore, the amplitude of the absorption peak P2 also increases with the increase of the diameter d of the metal disc. It should be pointed out that although the P2 peak shows a similar resonant behavior to the P1 peak. However, since the excitation position of the bright mode is the underlying array, the coupling strength of the P2 peak is lower than that of the P1 peak. Therefore, the amplitude of peak P2 is lower than that of peak P1 during the increase process of the diameter d, as shown in Fig. 5. For example, both the absorption peaks P3 and P4 are based on the bright-dark coupling effect between adjacent units (the resonance positions are 2.708THz and 3.416THz), as shown in Fig. 4 (a-b). During the process of increasing the diameter d of the metal disc, the coupling distance between the bright mode and the dark mode is rapidly reduced, thereby enhancing the coupling strength, resulting in the enhancement of the absorption peaks P3 and P4, as shown in Fig. 5. During the increase process of the diameter d of the metal disc, the resonant frequencies of the four absorption peaks are all reduced, as shown in Fig. 5. This is because the equivalent refractive index of the entire metasurface unit increases with the increase of the diameter d of the metal disk, according to formula (10). The equivalent refractive index is increased, and the corresponding resonant frequency is decreased. In addition, when the diameter d of the metal disc is equal to the lattice constant P, four absorption peaks are failed, and a new absorption band (with a bandwidth of 1.854THz and an absorption rate of 0.634) is obtained, as shown in Fig. 5. This metasurface acquires the conversion performance of absorption peak - absorption band. When the diameter d of the metal disc is equal to the lattice constant P, the top and bottom metal discs come into direct contact, forming a continuous porous metal layer. The coupling effect between these metal layers excites this absorption band.

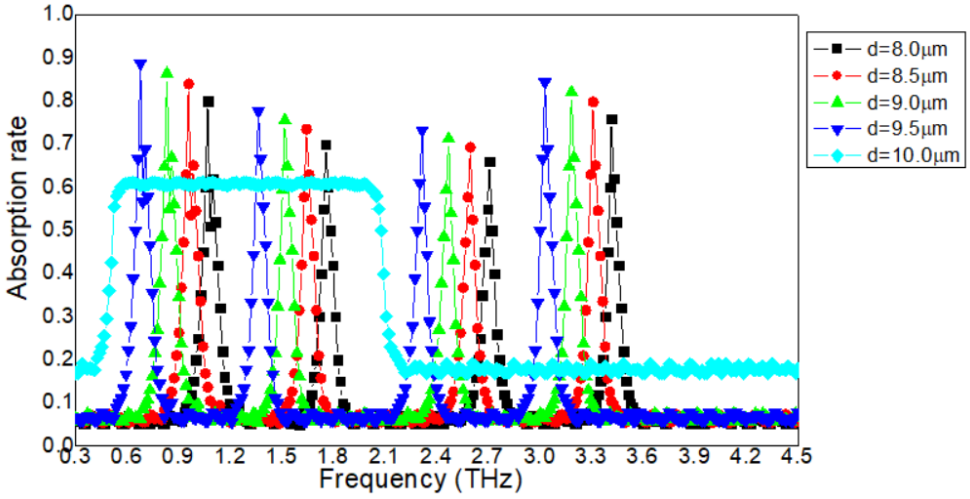

Fig. 5. Absorption spectra measured under different diameter conditions (colour online)

In the second group of experiments, the geometric parameter t2 was gradually increased, and the absorption spectrum is shown in Fig. 6. The absorption peaks P1 and P2 exhibit resonant behaviors that are inconsistent with those of P3 and P4. As the geometric parameter t2 is gradually increased, the amplitudes of the peaks P1 and P2 are rapidly decreased. When t2 is equal to 6.2 micrometers, the amplitude of peak P1 is 0.586 and that of peak P2 is 0.572. This is because the absorption peaks of P1 and P2 are both based on the vertical coupling effect between the upper and lower metal disc arrays. The intensities of these vertical couplings are gradually decreased as the geometric parameter t2 increases, thereby weakening the absorption peaks P1 and P2. In addition, peaks P1 and P2 were significantly shifted to the low-frequency region, with resonance positions of 0.412THz and 1.08THz, as shown in Fig. 6. On the contrary, the amplitudes of the P3 and P4 peaks were rapidly increased. When t2 is equal to 6.2 micrometers, the amplitude of peak P3 is 0.756, the amplitude of peak P4 is 0.843, and the resonance positions are 2.257THz and 3.112THz, as shown in Fig. 6. The absorption peaks P1 and P2 are based on the bright-dark coupling effect of the metal disc array in the horizontal direction. The intensities of these horizontal coupling effects will not be changed due to the increase of the geometric parameter t2. On the contrary, because the thickness of the dielectric layer is increased, the overall absorption performance of the metasurface sample is enhanced. Therefore, the amplitudes of the absorption peaks P1 and P2 are both increased, as shown in Fig. 6. In addition, since the overall equivalent refractive index of the metasurface structure increases with the increase of the geometric parameter t2, according to formula (10), the resonant frequencies of the four absorption peaks are all reduced, as shown in Fig. 6.

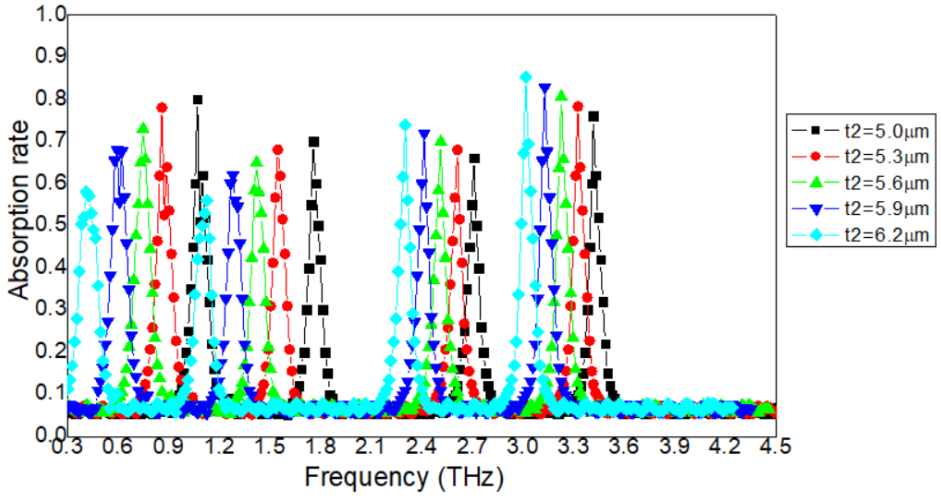

Fig 6. Absorption spectra measured under different thickness conditions (colour online)

In the third set of optimized measurements, the sensing performance and tunable performance of the metasurface sample were verified. The measurement results in Figs. 5 and 6 reveal the influence of the diameter of the disk array and the geometric parameter t2 on the performance of this metasurface. During the sample preparation process, changing the diameter of the disc or the geometric parameter t2 can have the effect of controlling the performance of the sample. However, such control strategies cannot adapt to the diverse demands in the industrial field. Therefore, it is necessary and meaningful to develop the tunable performance of this metasurface sample. In this measurement, all the geometric parameters remained unchanged, and the ambient temperature was gradually increased. The measurement results of the absorption rate are shown in Fig. 7. Such tunability is based on the inclusion of the temperature-sensitive material GST layer in the metasurface unit. The crystallinity of the GST layer is directly related to the temperature. The measurement results in Fig. 7 indicate that the absorption performance of the metasurface sample is gradually enhanced. Specifically, when the temperature reaches T=380K, the amplitudes of the absorption peaks are: 0.998, 0.925,0.867, 0.999, and the resonance points are: 2.082THz, 2.708THz, 3.706THz, 4.465THz, as shown in Fig. 7. This is because the equivalent refractive index is gradually reduced during the temperature increase process, thereby causing all absorption peaks to shift to the high-frequency region, as shown in Fig. 7. The sensitivity of this metasurface sample is:

$$S = \left| \frac{\Delta f}{\Delta T} \right| \tag{11}$$

The temperature difference is 80K, and the frequency differences at the four resonant positions are: 1.012THz, 0.952THz, 0.998THz, 1.049THz. According to Formula (11), the temperature sensing degrees of the four absorption peaks are: 0.013THz/K, 0.012THz/K, 0.012THz/K, 0.013THz/K, as shown in Fig. 7.

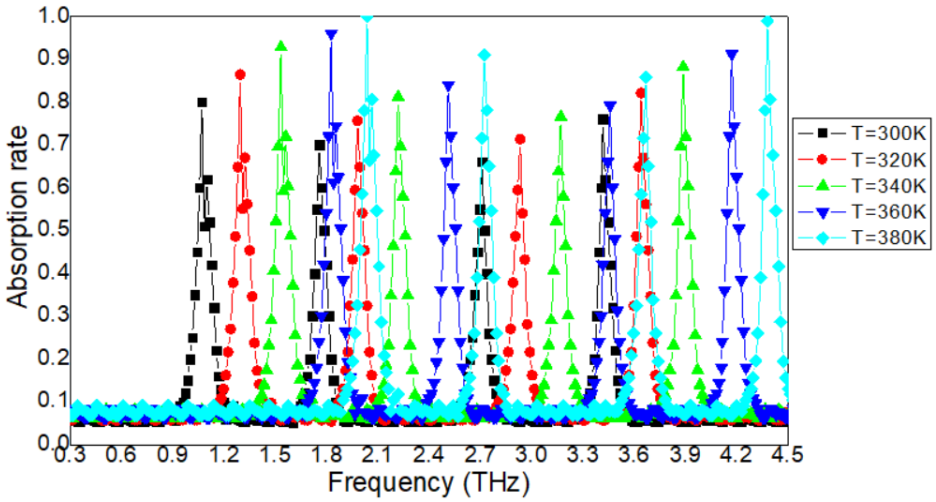

Fig. 7. Absorption spectra measured under different temperature conditions (colour online)

4. Conclusion

In this paper, a 6G terahertz metasurface sample was prepared and measured. In the range of 0.3-4.5THz, the metasurface sample obtained four absorption peaks with amplitudes of 0.811, 0.722, 0.663, and 0.764, and the resonance positions were 1.07THz, 1.756THz, 2.708THz, and 3.416THz. These absorption peaks are based on the bright-dark mode coupling effect between different disc metal arrays. Therefore, these absorption peaks exhibit sensitivity to geometric parameters. More importantly, in the experiment of temperature rise, the four absorption peaks were strengthened and moved to the high-frequency region. The metasurface sample exhibited obvious temperature sensitivity and tunability. This 6G terahertz metasurface sample has the potential to be applied to multimode resonant tunable 6G optoelectronic devices.

Declaration of interests

The authors declare that they have no known competing financial interests or personal relationships that could have appeared to influence the work reported in this paper.

Acknowledgments

This research was financially supported by Research Project on Higher Education Reform in Jiangsu Province in 2023: Exploration of the Path of "Digital Talent" Training for Urban Rail Transit Communication and Signal Technology Majors (2023JSJG194).

References

[1] Z. J. Zhang, L. L. Dai, Tsinghua Science and Technology **28**(5), 929 (2023).
[2] L. Dail, B.C. Wang, M. Wang, X. Yang, J. Tan, S. Bi, S. Xu, F. Yang, Z. Chen, M. Di Renzo, C. B. Chae, L. Hanzo, IEEE Access **8**, 45913 (2020).
[3] O. Buchnev, N. Podoliak, M. Kaczmarek, Nikolay I. Zheludev, Vassili A. Fedotov, Adv. Opt. Mater. **3**, 674 (2015).
[4] M. Q. Mehmood, S. Mei, S. Hussain, K. Huang, S. Y. Siew, L. Zhang, T. Zhang, X. Ling, H. Liu, J. Teng, A. Danner, S. Zhang, C. W. Qiu, Adv. Mater. **28**, 2533 (2016).
[5] Y. K. Srivastava, R. T. Ako, M. Gupta, M. Bhaskaran, S. Sriram, R. Singh, Appl. Phys. Lett. **115**, 151105 (2019).
[6] C. W. Tan Thomas, E. Plum, R. Singh, Adv. Opt. Mater. **8**, 1901572 (2020).
[7] X. B. Zhang, L. Wang, S. H. Tang, H. T. Cui, X. N. Xie, H. Wu, X. C. Liu, D. L. Yang, K. P. Wang, X. Ping, Opt. Fiber Technol. **75**, 103129 (2023).
[8] M. Papaioannou, E. Plum, E. T. F. Rogers, N. I. Zheludev, Light: Sci. Appl. **7**, 17157 (2018).
[9] Q. Huang, W. Zhu, Y. Wang, Z. Deng, Z. Li, J. Peng, D. Lyu, E. Lewis, M. Yang, Sensors Actuators B **321**, 128480 (2020).
[10] H. Y. Zebian, H. J. Taher, Opt. Fiber Technol. **54**, 112110 (2020).
[11] P. D. Hougne, M. F. Imani, T. Sleasman, J. N. Gollub, M. Fink, D. R. Lerosey, Sci. Rep. **8**, 6536 (2018).
[12] G. W Duan, J. Schalch, X. G. Zhao, A. B. Li, C. X. Chen, R. D. Averitt, X. Zhang, Sensors and Actuators A Physical **287**, 21(2019).
[13] D. R. Smith, S. Schultz, P. Markoš, C. M. Soukoulis. Phys. Rev. B **65**(19), 195104 (2001).
[14] H. Chen. Optics Express **20**(7), 7165 (2012).
[15] M. Wu, X. G. Zhao, J. D. Zhang, J. Schalch, G. W. Duan, K. Cremin, R. D. Averitt, X. Zhang, Applied Physics Letters **111**(5), 051101 (2017).
[16] H. Liu, K. Luo, S. Tang, D. Peng, F. Hu, L. Tu, Materials **11**(12), 2590 (2018).
[17] W. Fu, Y. Han, J. Li, H. Wang, H. Li, K. Han, X. Shen, T. Cui, Journal of Physics D **49**(28), 285110 (2016).
[18] A. Arbabi, A. Faraon, Scientific Reports **7**, 1 (2017).
[19] O. Buchnev, N. Podoliak, M. Kaczmarek, N. I. Zheludev, V. A. Fedotov, Adv. Optical Mater. **3**, 674 (2015).
[20] K. Appavoo, R. F. Haglund, Sci. Rep. **4**, 6771 (2014).
[21] G. Catalan, J. F. Scott, Advanced Materials **21**(24), 2463 (2009).
[22] M. R. Rakhshani, M. A. Mansouri-Birjandi, IEEE Sens. J. **16**, 3041(2016).
[23] P. Grahn, A. Shevchenko, M. Kaivola, New J. Phys. **14**, 093033 (2012).
[24] K. E. Oughstun, S. Shen, J. Opt. Soc. Am. B **5**, 2395 (1988).
[25] Z. C. Guo, K. H. Wen, Q. Y. Hu, W. H. Lai, J. Y. Lin, Y. H. Fang, Sensors **18**, 1348 (2018).
[26] D. R. Smith, S. Schult, P. Markos, C. M. Soukoulis, Phys. Rev. B **65**, 195104 (2022).

*Corresponding author: dengjianfang_2010@163.com